Polymer 293 (2024) 126625

Contents lists available at ScienceDirect

Polymer

journal homepage: www.elsevier.com/locate/polymer

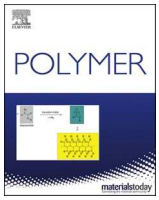

Characterization of nanoscale morphology and mechanical properties of conjugated polymer thin films dynamically exposed to a secondary solvent

Krystal L. House [a], Kent H. Christian [b], Thomas J. Emge [a], Haydee Pacheco [b], Richard A. Haber [b], Deirdre M. O'Carroll [a,b,*]

[a] Department of Chemistry and Chemical Biology, Rutgers University, Piscataway, NJ, USA
[b] Department of Materials Science and Engineering, Rutgers University, Piscataway, NJ, USA

A B S T R A C T

Solution processing techniques are often used to enhance intra and interchain order in semiconducting conjugated polymer thin films used in the active layer of organic optoelectronic devices. While there has been extensive research into the impact of solution processing on the local structural and electronic properties of these films, the nanomechanical properties of the films are less well understood and are challenging to characterize. We investigate the nanomechanical properties of conjugated polymer thin films arising from solution processing techniques. Our study relies on dynamic secondary solvent dripping to induce subtle changes to the film morphology. We examine thin films of P3HT, PCDTBT, PTB7, and PBDB-T-SF conjugated polymers, commonly used in organic photovoltaics, with the bimodal amplitude modulation-frequency modulation (AM-FM) imaging mode of the atomic force microscopy (AFM) viscoelastic method to probe their local physical and mechanical properties. We find that Young's Modulus data measured by AM-FM AFM can detect additional changes in film properties not discernible by other commonly used bulk thin-film characterization techniques. For PBDB-T-SF, we detect an increase in molecular order that is not noticable by UV–visible absorption spectroscopy, X-ray diffraction or nanoindentation. PCDTBT, the most amorphous of the polymers studied, shows no changes in absorption or X-ray diffraction data, yet clear changes in Young's Modulus were detected by AFM. On the other hand, increases in P3HT order that occurred due to dynamic secondary solvent dripping are detected in both the bulk and AFM measurements. Our study demonstrates the applicability of nanomechanical measurements for characterizing local structural variations in conjugated polymer films. This work is relevant to ongoing efforts to control and understand the complex structure-property-processing relationships of conjugated polymer thin films.

1. Introduction

We examine the alterations in the surface morphology and local mechanical properties of thin films of widely studied conjugated polymers: poly(3-hexylthiophene) (P3HT), poly[N-9′-heptadecanyl-2,7-carbazole-alt-5,5-(4′,7′-di-2-thienyl-2′,1′,3′-benzothiadiazole)] (PCDTBT), poly [[4,8-bis[(2-ethylhexyl)oxy]benzo[1,2-b:4,5-b']dithiophene-2,6-diyl][3-fluoro-2-[(2-ethylhexyl) carbonyl] thieno[3,4-*b*]thiophenediyl]] (PTB7), and poly[(2,6-(4,8-bis(5-(2-ethylhexylthio)-4-fluorothiophen-2-yl)-benzo[1,2-b:4,5-b']dithiophene))-alt-(5,5-(1′,3′-di-2-thienyl-5′,7′-bis(2-ethylhexyl)benzo[1′,2′-c:4′,5′-c']dithiophene-4,8-dione)] (PBDB-T-SF), arising from exposure to a secondary solvent during spin coating. Solution processing techniques are often used to enhance the intra- and inter-chain order of conjugated polymers in the active layer of organic optoelectronic devices [1]. Conjugated (i.e., semiconducting) polymers have been extensively studied for optoelectronic applications due to their diverse optical and electronic properties, which stem from the system of π-electrons created by the overlapping p-orbitals of alternating double and single bonds in their characteristic backbones [2]. However, semiconducting polymer materials generally exhibit lower device performance compared to inorganic semiconductors due to their relatively low crystallinity and complex film morphology [3–5]. In conjugated polymer thin films, the mobility of charge carriers is sensitive to the degree of intrachain and interchain order. Charge transport in conjugated polymers typically occurs both in the direction of the delocalized π-orbitals of the conjugated chain, (with charges hopping to neighboring π-orbitals in the π-π stacking direction), and along the chain-to-chain direction. The latter is relatively more difficult to achieve due to the presence of insulating alkyl chains [6–11]. Factors that have been shown to affect high-performance devices and charge mobility include highly ordered polymer chains, π-π stacking, molecular orientation, film morphology, and crystallinity [12–32]. Despite significant progress in understanding the properties of conjugated polymers, a crucial aspect that remains challenging to investigate is the nanoscale crystallization of these materials on going from solution to the solid state [33–36]. The ability to control and optimize this

* Corresponding author. Department of Materials Science and Engineering, Rutgers University, Piscataway, NJ, USA.
E-mail address: ocarroll@rutgers.edu (D.M. O'Carroll).

https://doi.org/10.1016/j.polymer.2023.126625
Received 10 July 2023; Received in revised form 6 November 2023; Accepted 23 December 2023
Available online 25 December 2023
0032-3861/

process is essential for achieving high-performance devices and unlocking the full potential of conjugated polymers in various fields.

Several techniques have been explored to improve the morphology, crystallinity, and charge transport properties of conjugated polymer films, [1,37–44]. Recent research has been focused on solution processing methods that can enhance intra- and inter-chain interactions. This approach has generated considerable interest due to its potential to achieve significant improvements in film formation through the incorporation of a secondary solvent, such as a poor solvent or antisolvent, or additives into polymer film processing methods [45,46]. Delayed evaporation rates that may be promoted by secondary solvents are believed to facilitate polymer assembly in some instances, leading to enhanced charge transport properties [47,48]. Moreover, solution phase studies of conjugated polymer self-assembly have shown that polymer aggregation in good solvent/poor solvent binary mixtures is strongly affected by the poor solvent polarity [49–51]. Several other studies have reported that solvent vapor exposure methods of polymer films using poor solvents, whether during pre-treatment [44], during spin coating [52], or after spin coating through solvent vapor annealing [53], can significantly enhance the charge transport properties of resultant devices. Incorporating secondary solvent additives into polymer precursor solutions [1,54–56] has also been shown to improve the morphology of a variety of conjugated polymer films by allowing for improved aggregation of the polymer during spin coating.

In our study, we focus on a particular solution processing approach: the antisolvent dripping method [57,58], which has been widely used for several years to enhance the performance of inorganic-organic hybrid perovskite films [57–62]. Jo et al. demonstrated that a similar method can impact the morphology and charge transport of conjugated polymer films [63]. By combining a good solvent and a poor solvent in various ratios to create cosolvent systems, they systematically studied the effects of polarity, viscosity, and solubility of secondary solvents added after spin coating on poly (3-hexylthiophene) (P3HT) thin films. Jo et al. determined that increasing solvent solubility enhanced the molecular ordering of the films. Further, the morphology and charge transport properties were increasingly altered with decreasing solvent polarity and viscosity.

In our study, we investigate the subtle changes in the local physical and mechanical properties of several common conjugated polymer thin films, including P3HT, PCDTBT, PTB7, and PBDB-T-SF, exposed to a poor/secondary solvent *during* the spin coating process (rather than before or after, like in previous methods). The advantage to adding the secondary solvent during the process is that it shortens the treatment time and number of process steps required [64]. Initially, we selected the very well-studied conjugated polymer, P3HT, as well as three additional conjugated polymers (PCDTBT, PTB7, and PBDB-T-SF), known for their higher reported efficiencies in organic photovoltaic devices, including one that is often used in fullerene-free devices (PBDB-T-SF), see Fig. 1 [65]. The lower frontier orbital energy levels of these polymers lead to advantages over standard materials, including longer wavelength absorption and improved ambient stability. In contrast to the cosolvent systems used in previous work, we chose a high boiling point good solvent to prepare the polymer precursor solution to ensure this solvent remains long enough during spin coating to allow for mixing with the poorer (secondary) solvent added during spin coating.

It is necessary to choose robust and complementary methods of characterizing subtle changes in morphology promoted by solvent treatment to enable investigation of the physical, optical and mechanical properties of conjugated polymer films in parellel. While several complementary methods are available to characterize order in conjugated polymer films, they are often insensitive to amorphous domains: X-ray diffraction, for instance, only probes the bulk (semi)crystalline properties of the film. Atomic force microscopy, on the other hand, can map the elastic and viscoelastic properties of materials at the nanoscale, making it an essential tool in polymer research [34,66–82]. Furthermore, from the many nanomechanical mapping modes available, bimodal AFM techniques such as AM-FM viscoelastic mapping provide fast, high-resolution topography and nanomechanical properties simultaneously [83]. Despite its powerful capabilities, the high-resolution viscoelastic mapping potential of bimodal AFM is still widely underutilized in conjugated polymer research.

In this study, we investigate the nanomechanical properties of conjugated polymer films by utilizing atomic force microscopy (AFM) AM-FM viscoelastic mapping. We compare the results obtained from AFM with those obtained using more common characterization techniques such as UV–visible absorption spectroscopy (UV–vis), grazing-incidence X-ray diffraction (GIXRD), and nanoindentation. Our focus is on demonstrating the advantages of nanoscale structural and mechanical measurements using AFM for the characterization of subtle changes in film morphology that may be missed using other techniques. Through this work, we aim to contribute to the ongoing efforts in conjugated polymer research to develop thin films with defined structure, molecular (especially chain) orientation, packing and crystallinity by applying a sensitive nanomechanical characterization approach.

2. Materials & methods

2.1. Materials

The molecular structure of the four conjugated polymers studied are

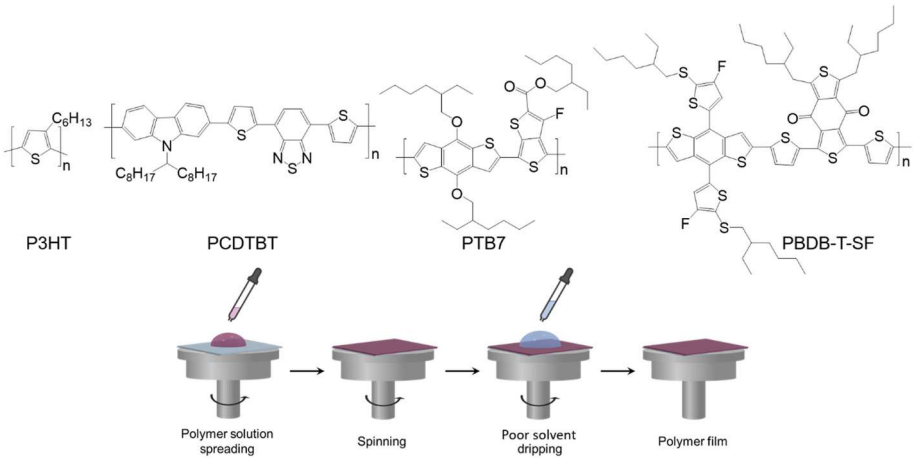

Fig. 1. Molecular structures of polymers (P3HT, PCDTBT, PTB7, PBDB-T-SF) and schematic illustration of poor (secondary) solvent dripping spin-coating process for conjugated polymer thin films.

shown in Fig. 1. Poly(3-hexylthiophene) (P3HT) regioregular (electronic grade, MW = 58000, PDI = 2.4) was purchased from Rieke Metals. Poly [N-9′-heptadecanyl-2,7-carbazole-alt-5,5-(4′,7′-di-2-thienyl-2′,1′,3′-benzothiadiazole)] (PCDTBT) (MW = 31838, PDI = 6.1) and Poly [[4,8-bis [(2-ethylhexyl)oxy]benzo[1,2-b:4,5-b']dithiophene-2,6-diyl][3-fluoro-2-[(2-ethylhexyl)carbonyl]thieno[3,4-*b*]thiophenediyl]] (PTB7) (MW = 23556, PDI = 2.93) were purchased from Lumtec. Poly[(2,6-(4,8-bis (5-(2-ethylhexylthio)-4-fluorothiophen-2-yl)-benzo[1,2-b:4,5-b']dithiophene))-alt-(5,5-(1′,3′-di-2-thienyl-5′,7′-bis(2-ethylhexyl)benzo[1′,2′-c:4′,5′-c']dithiophene-4,8-dione)] (PBDB-T-SF) (MW = 58194, PDI = 3.17) was purchased from Ossila. Chlorobenzene and toluene were purchased from Sigma Aldrich and used as received.

2.2. Thin-film fabrication

Glass substrates were precleaned by sonication in a detergent solution (Sparkleen, Fisherbrand), submersion in an ethanol/HCl (1:1) solution, and sonication in isopropanol, each for 10 min. The substrates were rinsed three times with deionized water between each step. Silicon (Si) substrates were precleaned by sonication in a detergent solution and submersion in a hot water/ammonium hydroxide/peroxide (5:1:1) solution, each for 10 min. The substrates were rinsed three times with deionized water between each step. Thin films were fabricated by dynamic spin coating of polymer dissolved in chlorobenzene (20 μL) followed by toluene (10 μL) added during spin coating. A schematic of the poor (secondary) solvent dripping method used for film preparation is shown in Fig. 1. For P3HT (30 mg mL^{-1}) and PBDB-T-SF (20 mg mL^{-1}), films were prepared at 3000 rpm for 20 s, with toluene added after 15 s. Due to substantial removal of the film by toluene, for PTB7 (40 mg mL^{-1}) and PCDTBT (40 mg mL^{-1}), films were prepared at 3000 rpm for 40 s with a second addition of polymer after 20 s, spin speed was increased to 6000 rpm for 6 s with toluene added after 3 s. All films were dried under vacuum overnight prior to characterization and stored under vacuum before additional characterization.

2.3. Solvent selection

Good and poor solvents for the conjugated polymers and acceptors were selected for this work based on Hansen Solubility Parameters (HSP) [84]. Solubility parameters, sometimes called cohesion energy parameters, are derived from the energy of vaporization. Hildebrand and Scott were the first to use the term *solubility parameter* [85,86]. The Hildebrand solubility parameter, δ, is defined as the square root of the cohesive energy density, shown in Eq. (1)

$$\delta = (E/V)^{1/2} \tag{1}$$

Where V is the molar volume of the pure solvent, and E is its total energy of vaporization. Hansen extended this work by breaking up the total cohesive energy (E) into its individual parts of energy from dispersion forces (E_D), dipolar intermolecular force (E_P), and hydrogen bonding (E_H), shown in Eq. (2).

$$E = E_D + E_P + E_H \tag{2}$$

The square of the Hildebrand solubility parameter is thus the sum of the squares of the Hansen parameters divided by the molar volume, shown in Eqs. (3) and (4).

$$\frac{E}{V} = \frac{E_D}{V} + \frac{E_P}{V} + \frac{E_H}{V} \tag{3}$$

$$\delta^2 = \delta_D^2 + \delta_P^2 + \delta_H^2 \tag{4}$$

Where δ_D, δ_P, δ_H and are the HSP from dispersion forces, dipolar intermolecular force, and hydrogen bonding, respectively. HSP were used for this work since they have been shown to be useful when predicting the solubility behavior of organic semiconductors [87–90]. Materials with similar HSP have high affinity for each other, so the solubility parameter distance, or interaction radii, R_a, between two materials is used to determine good and poor solvents for each polymer and acceptor with good solvents having a smaller R_a, thus a stronger interaction, with a given solute, as shown in Eq. (5) [84].

$$R_a^2 = 4(\delta_{D1} - \delta_{D2})^2 + (\delta_{P1} - \delta_{P2})^2 + (\delta_{H1} - \delta_{H2})^2 \tag{5}$$

Where δ_{D1}, δ_{P1}, δ_{H1} are the HSP for the first material and δ_{D2}, δ_{P2}, δ_{H2} are the HSP for the second material. HSP for the polymers in this work were estimated using a modified Van Krevelen group contribution method [91–93], see Table 1. The HSP for the solvents were taken from literature sources [93]. The group contribution theory was used to estimate the HSP because experimental determination of HSP using solubility values is material consumptive. Though experimental HSP are available for P3HT, which agree well with the calculated values, calculated values were used for all polymers for uniformity.

Table 2 below gives the R_a values for each polymer with various solvents. Conducting experimental trials to determine good and poor solvents for a specific polymer leads to the identification of a sphere with a given radius, denoted as R_0, encompassing all the good solvents. Solvents are categorized as 'poor solvents' when the difference between the solubility parameters of a particular solvent and the polymer exceeds the radius of the corresponding Hansen sphere ($R_a > R_0$). Although comprehensive solubility tests were not undertaken in this study, the literature reports R_0 values for P3HT ranging from 1.2 to 3.6 $MPa^{0.5}$ [87,94,95]. It is important to note the challenges in determining precise solubility parameters for polymers due to uncertainties in molecular weight. For the scope of this work, 'poor solvents' for P3HT are defined as those resulting in an R_a value equal to or greater than 3.6 $MPa^{0.5}$. The poor solvents in Table 2 were screened by measuring the changes in UV–vis absorption spectra of P3HT films prepared with and without solvent treatment. The worst solvents had no effect on the optical properties of P3HT films, while toluene and methylene chloride, with lower R_a values, both affected the optical properties of P3HT.

Toluene was chosen as the secondary solvent for all the polymers since it had the greatest effect on the optical properties of P3HT. Though the calculated R_a values were different for each polymer, they were found to follow a similar trend where the lowest R_a values correspond to good solvents, and higher R_a values correspond to poor solvents for each polymer.

2.4. UV–visible absorption spectroscopy (UV–vis)

UV–vis absorption spectra were performed using an S.I. Photonics CCD array spectrophotometer with deuterium and tungsten lamps. The minimum wavelength was set at 300 nm, and the maximum was set at 900 nm, with the lamp crossover wavelength set 350 nm, except for PCDTBT, which was set to a 450 nm crossover in order to preserve a peak of interest.

2.5. Grazing-incidence X-ray diffraction (GIXRD)

GIXRD data were obtained, as described previously [37], using a Bruker Vantec-500 area detector and a Bruker FR571 rotating-anode X-ray generator operating at 40 kV and 45 mA, and equipped with a 3-circle Azlan goniometer. The system used a 0.5 mm pinhole

Table 1
Hansen solubility parameters (HSPs) calculated for each polymer using a modified group contribution method [91–93].

Polymer	δ_d	δ_p	δ_h
P3HT	18.5	4.1	4.2
PCDTBT	20.0	3.7	9.3
PTB7	22.4	2.7	5.3
PBDB-T-SF	27.2	3.0	4.5

Table 2
Summary of the calculated Hansen solubility parameter distance (R_a) between the indicated polymers with selected solvents.

Solvent	P3HT	PCDTBT	PTB7	PBDB-T-SF
Acetone	9.1	11.5	15.9	24.7
Benzyl Benzoate	3.3	4.3	5.4	14.6
Benzyl chloride	3.5	7.9	8.9	17.4
Butyl Benzoate	2.0	5.4	8.7	18.0
Chlorobenzene	2.4	7.6	7.7	16.6
2-Chlorotoluene	2.3	7.4	7.8	16.7
1,2-Dichlorobenzene	2.8	6.7	7.6	16.4
Diethyl Ether	8.1	12.0	15.8	25.4
Dimethylformamide	12.1	11.5	16.0	23.3
Dimethylsulfoxide	13.7	13.1	16.6	22.8
Hexane	9.3	14.3	16.1	25.2
Methanol	21.3	18.9	24.9	32.1
Methylene Chloride	5.3	7.3	11.9	21.0
2-Propanol	13.5	11.3	17.6	25.9
Toluene	3.6	8.6	9.5	18.6

collimation and a Rigaku Osmic parallel-mode mirror monochromator (Cu Kα; λ = 1.5418 Å). Data were collected at room temperature with a sample to detector distance of 10 cm. Data collection was carried out using Bruker GADDS v.4.1.51 (2015) software. Data were collected with the sample surface nearly parallel to the source beam, or grazing-incidence, with out-of-plane diffraction geometry. For GIXRD measurements, the films were prepared as previously described [30] on a Si wafer substrate rather than SiO_2 glass, in order to eliminate the large background counts due to the amorphous scattering of the glass.

2.6. Nanoindentation

Nanoindentation (NanoTest Vantage) was also used for nanomechanical characterization of the pristine and treated polymer films. A 10 × 10 grid of indents (and a 15 μm offset) with a maximum load of 20 μN was made using a Berkovich diamond indenter. The Oliver-Pharr model was used to analyze the load-displacement curves for the estimation of the hardness and elastic modulus [96]. The Young's modulus was calculated using the elastic modulus and Poisson's ratio for the diamond indenter, (1140 GPa and 0.07 respectively), and a Poisson's ratio of 0.35 for the polymer films, which is the estimated value typically used for polymeric materials [97–99].

2.7. Atomic force microscopy (AFM)

AFM measurements were done using an Asylum Research Cypher ES Atomic Force Microscope. The measurements were performed under ambient conditions in the sealed AFM enclosure. Silicon cantilevers with a Cr/Au reflex coating (AC160TSA-R3, Oxford Instruments, USA) with nominal spring constant of 26 N/m and nominal tip radius of 7 nm were used. Before each measurement, the probes were calibrated using GetReal™ automated probe calibration provided by Asylum Research. This calibration procedure calculates the spring constant and inverse optical lever sensitivity of the probe in one step using the probe characteristics with the well-known thermal noise [100] and Sader's method [101].

AFM images were acquired by operating the AFM in AM-FM mode. This technique, developed by Asylum Research, is used to measure the viscoelasticity of materials. BlueDrive™ photothermal excitation [102] is used to excite the cantilever simultaneously at two frequencies. The first resonance is operated in amplitude modulation (AM) mode and is used for tapping mode topography and phase images. The higher resonance mode is operated in frequency modulation (FM) mode and is used to calculate the elastic modulus [103]. While a reference sample of known modulus can be scanned to determine quantitative elastic modulus values, here default parameters were used to achieve a qualitative modulus comparison between the pristine and toluene treated films of each polymer, and a reference high-density polyethylene (HDPE) sample was scanned before, during, and after pristine/treated film measurements to ensure low variation in the imaging. A new tip was used for each pristine/treated pair of films. A digital resolution of 256 lines × 256 points and a scanning rate of 2.00 Hz were used.

3. Results and discussion

3.1. UV–visible absorption spectroscopy

The effects of toluene treatment on the optical properties of pristine and treated conjugated polymer films were investigated using UV–visible absorption spectroscopy (Fig. 2A–D). Both pristine and treated films exhibit characteristic absorption peaks attributed to π-π* electronic transitions and, in some cases, vibronics thereof. For PCDTBT, the spectra of the pristine and treated films showed no significant differences in the peak positions or intensities. On the other hand, for P3HT and PTB7, the longer wavelength peaks increased in intensity relative to the shorter wavelength peaks for the treated films compared to the pristine films (Fig. 2A–C). This increase in intensity is attributed to a slight increase in the ordering of polymer chains within the films, which was reported previously in the literature [2,10,53,104–109].

In contrast, for PBDB-T-SF, the longer wavelength peak of the treated film was slightly reduced in intensity relative to the shorter wavelength peaks (Fig. 2D). Although the changes observed in the absorption spectra were subtle, they suggested that changes to the film morphology occurred as a result of toluene treatment. These changes might be related to the ability of toluene to selectively extract lower molecular weight chains from the polymer matrix, resulting in a more ordered polymer chain arrangement within the film.

3.2. X-ray diffraction

The bulk crystallinity of pristine and toluene-treated conjugated polymer films was investigated using grazing-incidence XRD (GIXRD), and the out-of-plane data are presented in Fig. 3. The pristine P3HT film exhibited a (100) diffraction peak at a 2θ value of 5.4°, indicating a lamellar structure from intermolecular alkyl chain stacking [110], as well as the higher order (200) and (300) diffraction peaks, indicating highest crystallinity along the alkyl chain stacking direction (Fig. 3A). A weak (010) diffraction peak, attributed to in-plane intermolecular π–π stacking, was observed around 23.8°. The treated film showed a shift in the (100) peak to a higher diffraction angle, 5.5°, indicating a decrease in the *d*-spacing in the alkyl chain stacking direction with toluene treatment. However, the *d*-spacing for the in-plane π–π stacking remains the same, within experimental error. These results suggest structural changes occur predominantly, if not entirely, along the alkyl chain direction with toluene treatment.

In contrast, the absence of well-defined diffraction peaks for pristine or treated PCDTBT films (Fig. 3B) indicates the disordered, amorphous structure of the PCDTBT polymer film. Differences between the pristine and treated film cannot be determined as the signal is too low to be distinguished from noise. In the literature, similar broad, diffuse scattering at a 2θ value of ~24° has been observed for amorphous PCDTBT films [111,112].

The GIXRD patterns for pristine and treated PTB7 films showed two diffraction peaks, attributed to the (100) and (010) diffraction peaks (Fig. 3C). The intensities of both peaks decreased in the treated film, partially due to the reduction in film thickness after toluene treatment. However, the intensity of the (100) peak in the treated film was ~53 % of that for the pristine film, while the intensity of the (010) peak was only ~26 % of the intensity of that for the pristine film. This suggests, upon toluene treatment, there is either an increase in order in the alkyl chain direction or a decrease in order in the π–π stacking direction. The pristine PBDB-T-SF film exhibited a peak at a 2θ value of ~24.4° attributed to the (010) peak (Fig. 3D). The absence of any well-defined

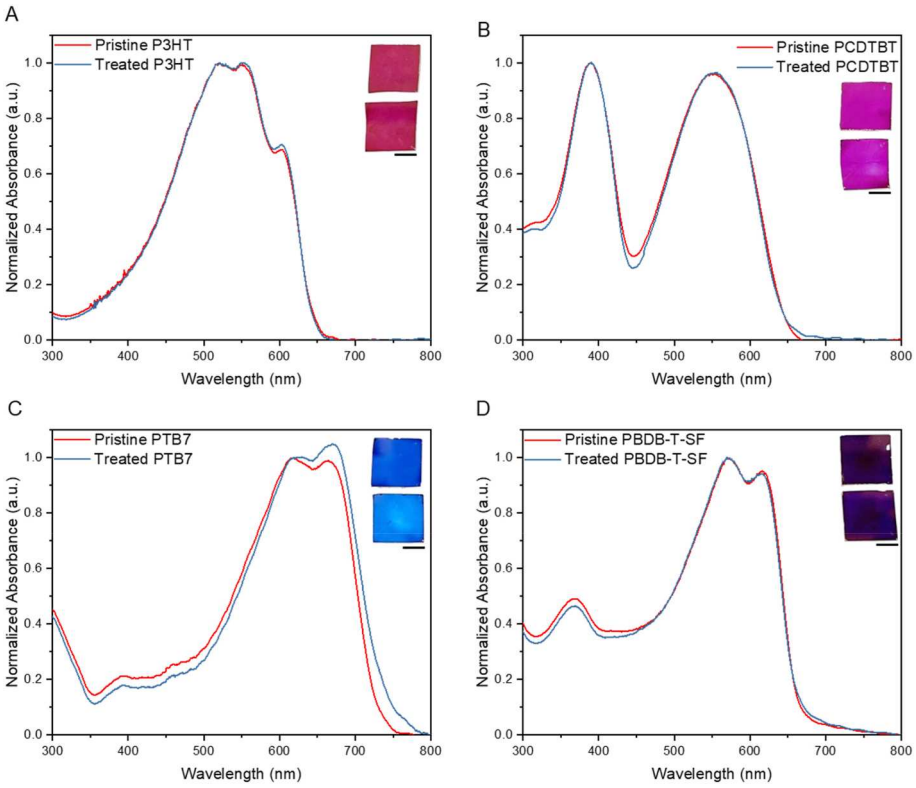

Fig. 2. (A–d) Normalized UV–visible absorption spectra of pristine (red) and toluene-treated (blue) A) P3HT, B) PCDTBT, C) PTB7, and D) PBDB-T-SF on glass substrates, respectively. The spectra for PTB7 and PBDB-T-SF were baselined at a wavelength of 800 nm, and, due to oscillations in the spectra, at the average intensity from 750 to 800 nm for P3HT and PCDTBT prior to normalization at the first π–π* absorption peak. Insets: Pictures of prepared films – pristine (top), treated (bottom). The black scale bar is 5 mm. (For interpretation of the references to color in this figure legend, the reader is referred to the Web version of this article.)

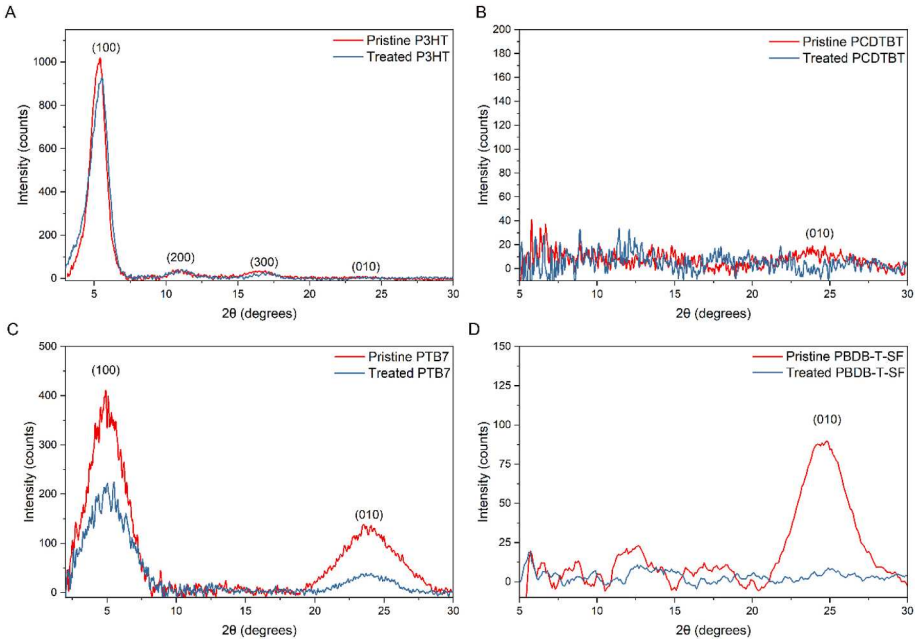

Fig. 3. GIXRD patterns of pristine (red) and toluene-treated (blue) A) P3HT, B) PCDTBT, C) PTB7, and D) PBDB-T-SF on Si substrates. All GIXRD patterns were baselined using baseline subtraction from OriginLab [116]. A user-defined baseline model was used, and anchor points connected by interpolation were chosen to preserve the peaks in the patterns. The profiles where smoothed using a 5-point adjacent averaging procedure. (For interpretation of the references to color in this figure legend, the reader is referred to the Web version of this article.)

peaks for the treated film suggests significantly lower intermolecular ordering after toluene treatment.

Conjugated polymers can take on several orientations in films. Our out-of-plane GIXRD results are consistent with the literature, where P3HT has a preferential edge-on orientation [113], PCDTBT is amorphous [111], PTB7 shows both orientations with a moderate preference

for face-on orientation [114],and PBDB-T-SF shows a preferred face-on orientation [115]. Since these data were weak, and the in-plane data were expected to be even weaker, the collection of in-plane data was not attempted. The GIXRD results suggest that toluene treatment can induce molecular-level structural changes in the conjugated polymer films, which may affect their performance in device applications.

3.3. Nanoindentation

Nanoindentation measurements were performed to examine the nanomechanical properties of the pristine and treated polymer films on glass substrates and to compare the results with the AFM nanomechanical data. Previously, it has been shown that higher crystallinity of conjugated polymer films has led to a larger modulus value [117]. The Young's modulus and hardness measured by nanoindentation for each film are shown in Table S1. The values are much higher than would be expected for these films, indicating a substantial effect from the glass substrate [76,99,118]. This substrate effect has been demonstrated in the literature for conjugated polymer films. PCDTBT and PTB7 show a significant increase in Young's modulus with toluene treatment. This is likely due to a more significant effect from the substrate as the treated films for these polymers were much thinner than the pristine films. The thickness of each film was measured using AFM and can be found in Table 3. To obtain accurate mechanical data from nanoindentation, thicker polymer films or advanced nanoindentation techniques are required [76]. In contrast with the nanoindentation results, the AFM nanomechanical measurements reported below do not exhibit substrate effects and produce nanomechanical data that is consistent with bulk values previously reported for such conjugated polymers.

3.4. Atomic force microscopy

AM-FM AFM imaging was used to investigate the surface morphology and nanomechanical properties of the pristine and treated polymer films. Figs. 4–7 show representative 1 μm × 1 μm topography, phase, and Young's modulus images for each of the pristine (A-C) and treated (D-F) films. The scale of the images was varied between the pristine and treated films to ensure the features of each image could be properly visualized. Figures with uniform scale bars can be found in the Supplementary Information (Figs. S1–S4). The AFM images showed that the mechanical properties of the polymers varied on the nanoscale and were particularly apparent for P3HT and PBDB-T-SF. The individual grains and grain boundaries could be seen, and film uniformity was broken at the grain boundaries where a maximum modulus value was obtained. We found that solvent treatment notably altered the film morphology of PBDB-T-SF. Enlarged phase images of the treated film showed smaller features and highly ordered rodlike structures of the polymer, indicating an increase in order in the film morphology (Fig. 8A and B).

3.4.1. Roughness

Surface roughness is an important factor that affects the properties of materials at the nanoscale. In this study, root-mean-squared (RMS) roughness was determined for 1 μm × 1 μm topography images, taken in at least 16 different areas, for both pristine and treated films. The mean values are presented in Table 3. It is important to note that no evidence of dewetting was observed in the numerous areas assessed. Given that the RMS roughness is significantly smaller than the measured film thickness, also presented in Table 3, there is no apparent indication of dewetting. Film thickness was measured using AFM imaging. A scratch was used to remove the film from the glass substrate, creating a distinct step-like feature that was then scanned. The average height of this step was determined by conducting four separate scans across different regions of the scratch.

The results indicate that P3HT films have a much higher roughness compared to films of the other polymers. This is attributed to the greater crystallinity of P3HT than the other polymers tested. To ensure uniformity of the measurements, RMS roughness was also determined for topography images of a reference HDPE sample, which was imaged along with each of the four pristine/treated polymer film sets. A minimum of three 1 μm × 1 μm areas were measured before, during, and after each of the sets, for a total of at least nine images per set. No significant difference was found using a two-sample *t*-test between the RMS roughness values of the reference sample measurements imaged with each set. However, the difference between the RMS roughness of the pristine and treated films was found to be statistically significant using a two-sample *t*-test for P3HT, PTB7, and PBDB-T-SF. Among these, only PTB7 showed an increase in RMS roughness with toluene treatment. The RMS roughness decreased with toluene treatment for both P3HT and PBDB-T-SF, suggesting a more uniform film. PCDTBT, the most amorphous film, did not show a statistically significant difference in RMS roughness between the pristine and treated films.

In summary, the results indicate that the RMS roughness values are

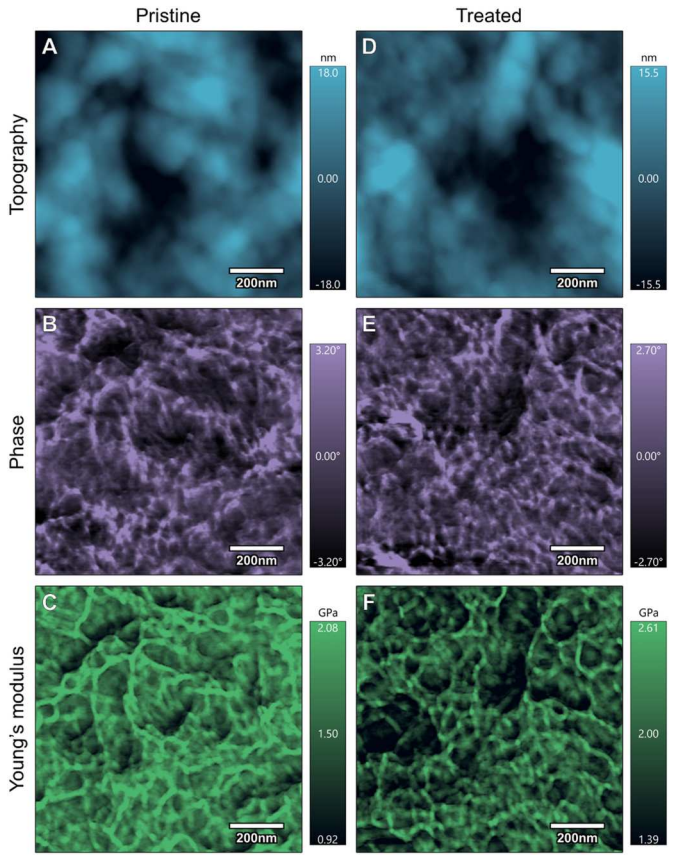

Fig. 4. Topography (A, D), phase (B, E), and Young's modulus (C, F) AFM images of pristine (A–C) and toluene treated (D–F) P3HT thin films.

Table 3
Film thickness and root mean squared (RMS) roughness of pristine and treated P3HT, PCDTBT, PTB7, and PBDB-T-SF films from AFM topography images. A minimum of four areas of a scratch made through the film were measured for thickness, and a minimum of 16 1 μm × 1 μm images were used for RMS roughness.

Polymer	Film Thickness, nm		RMS Roughness, nm	
	Pristine	Treated	Pristine	Treated
P3HT	156 ± 14	121 ± 10	10 ± 2	8 ± 1
PCDTBT	129 ± 8	60 ± 6	0.9 ± 0.1	0.8 ± 0.2
PTB7	126 ± 12	55 ± 3	0.7 ± 0.1	0.9 ± 0.2
PBDB-T-SF	222 ± 23	251 ± 42	1.1 ± 0.2	1 ± 0.2

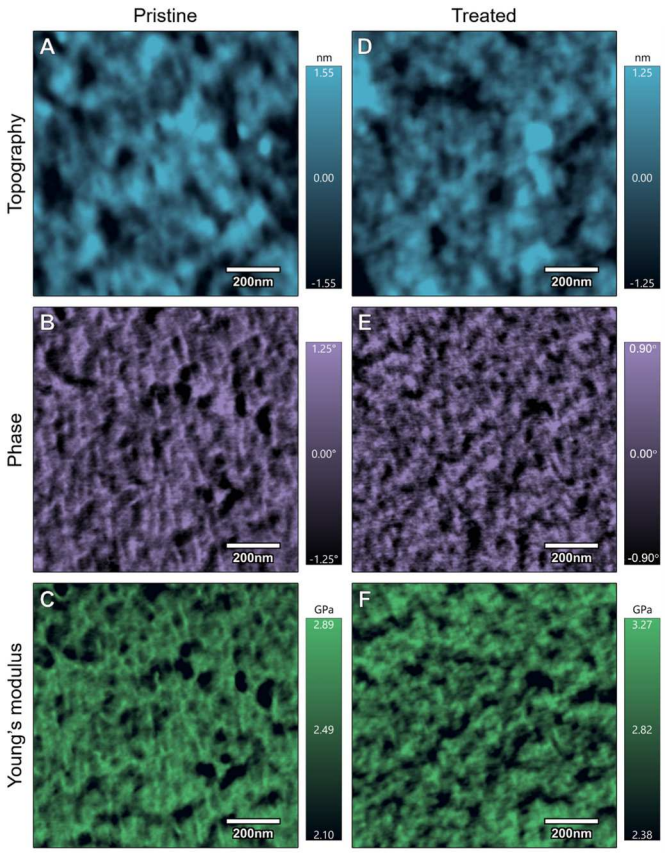

Fig. 5. Topography (A, D), phase (B, E), and Young's modulus (C, F) AFM images of pristine (A–C) and toluene treated (D–F) PCDTBT thin films.

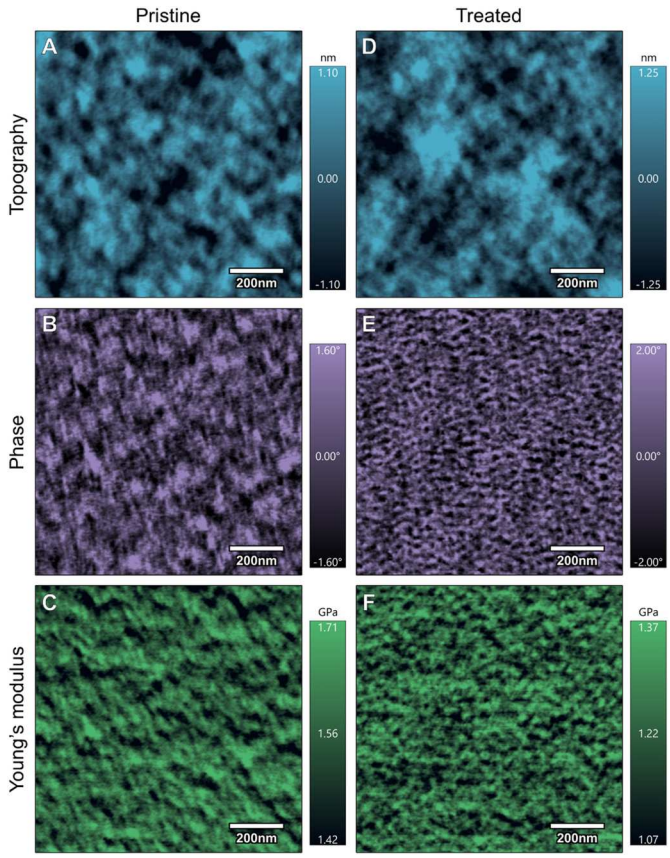

Fig. 6. Topography (A, D), phase (B, E), and Young's modulus (C, F) AFM images of pristine (A–C) and toluene treated (D–F) PTB7 thin films.

influenced by the crystallinity and uniformity of the films, and toluene treatment can affect the RMS roughness values of certain polymers. These findings provide valuable insights into the surface properties of these polymers and can help guide the optimization of their processing and performance in various applications.

3.4.2. *Feature size*

Feature size analysis was conducted using AFM phase images, which provide excellent contrast between features without being influenced by the height of the features. The term 'feature size' is used here to describe the specific structural characteristics of interest to this study that are present in the non-crystalline organic films under investigation. These characteristics may involve grains or domains within the film, variations in film morphology, or other non-crystalline structural elements. Quantifying the feature size facilitates the analysis of these non-crystalline features. To isolate the features in them images, the phase images were flattened so that the offset or center of the phase range of the image would be 0°. A color scale was created to highlight any grains with a phase above the mid-point. Using ImageJ [119], a minimum of five images for each film were set to 8-bit grayscale, and a threshold was selected so that every pixel below a pixel value of 170 were set to black (0-pixel value), and those over were set to white (255-pixel value). Although this pixel value ensured that most higher phase features were separated, some features remained connected and artificially large, while others were made artificially small due to the complexity of the images. Nevertheless, the same thresholding value was selected for every image, allowing for a suitable comparison between pristine and treated films.

The feature size analysis revealed interesting differences between the pristine and treated films (Fig. 9A–D). The size distribution of higher phase features for each film was approximately lognormal, and a normal distribution fit to the log of the feature size was shown for each film. To compare the maximum of the distribution for each pristine and treated pair, the bin sizes of each histogram were selected. Using a two-sample *t*-test, a statistically significant difference in mean feature size was observed only for the PBDB-T-SF films, with a subtle decrease in higher phase feature size for the toluene-treated film compared to the pristine film. While the other films did not show statistically significant differences in feature size between the pristine and treated samples, visual inspection of the images suggests that there may be subtle changes in the distribution and morphology of the features, particularly for P3HT and PTB7. Further investigation with additional characterization techniques could shed more light on these observations.

3.4.3. *Nanomechanical properties*

The analysis of the Young's modulus images for the pristine and treated P3HT, PCDTBT, PTB7, and PBDB-T-SF films are shown in Fig. 10A–D. When interpreting AM-FM nanomechanical data, certain considerations and limitations must be acknowledged. Notably, it is important to consider the viscoelastic nature of the sample [120]. Establishing connections between surface adhesive and viscoelastic properties to measured bimodal AFM data is an area of ongoing research [121].

The primary source of error in these measurements is often attributed to the model employed to characterize the contact area between the AFM tip and the sample, particularly with viscoelastic materials. Minimizing this error is possible by employing relatively small indentations. The AM-FM technique, known for its application of small forces during imaging, induces minimal sample deformation. Representative indentation images, illustrating the small indentations utilized for each film, are available in Figs. S5–8. While this study avoids claims of quantitative precision, it is notable that numerical simulations in the literature have

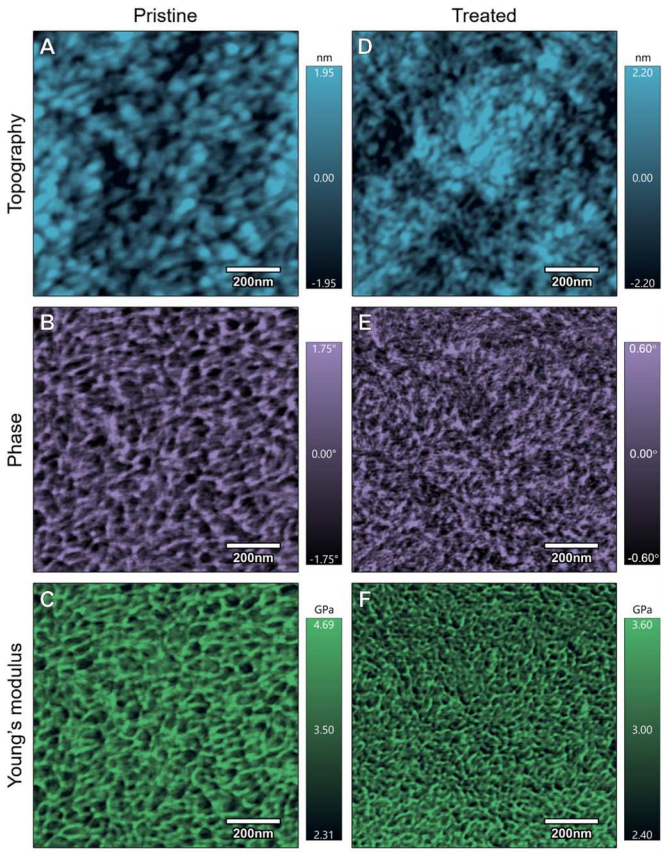

Fig. 7. Topography (A, D), phase (B, E), and Young's modulus (C, F) AFM images of pristine (A–C) and toluene treated (D–F) PBDB-T-SF thin films.

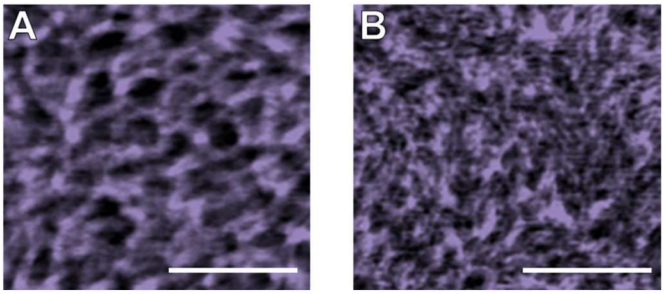

Fig. 8. Enlarged AFM phase images of pristine (A) and toluene treated (b) PBDB-T-SF thin films. The scale bar is 200 nm.

validated the accuracy of Young's modulus values measured using bimodal AM-FM across a diverse range of materials, spanning from 1 MPa to 100 GPa [122].

Moreover, the influence of environmental factors, particularly during measurements conducted in air, as executed in this study, must be acknowledged. Adhesion measurements are significantly impacted by relative humidity, as capillary forces can dominate the measured adhesion. Nevertheless, studies have shown that Young's modulus measurements exhibit relatively low sensitivity to changes in relative humidity [75].

Furthermore, it is important to recognize that the elastic modulus acquired through AM-FM imaging primarily reflects the surface properties of the material rather than providing insights into the bulk of the film. Establishing a correlation between viscoelastic properties in the bulk and those on the surface, which can be influenced by factors like fitting models, oscillation frequency, and the presence of defects in bulk samples, remains a challenging and actively researched area [123–125].

Here, nanomechanical properties were analyzed by preparing histograms of the calculated Young's modulus at each pixel of the images (256 × 256 pixels) for a minimum of 16 images in four different areas for each film. For the P3HT films (Fig. 10A), toluene treatment increased both the average Young's modulus and the full width at half maximun compared to the pristine film, suggesting a shift to more ordered or polycrystalline films. In the case of PCDTBT films (Fig. 10B), there are two different domains with different modulus parameters. The peaks at higher Young's modulus correspond to more crystalline domains, while those at lower Young's modulus correspond to more amorphous domains. In the pristine film, there are two distinct peaks in the amorphous domain, while peaks in the crystalline domain are broader. In the treated film, there is a larger variation in the crystalline domain, as these peaks are very broad, and the amorphous domain has one strong, sharp peak. The modulus value of the amorphous domain is similar for both the pristine and treated film; however, the crystalline domain in the treated film moves to higher modulus values.

For the PTB7 films, shown in Fig. 10C, each resulted in asymmetrical distributions. For the pristine film, the Young's modulus skewed towards higher, more crystalline values. While for the treated film, the Young's modulus skewed towards lower, more amorphous values. There are two different domains for the PBDB-T-SF films, shown in Fig. 10D. Compared to the treated films, the pristine films appear more amorphous, while the increase in Young's modulus for the treated film points to an increase in film crystallinity. Interestingly, the nanomechanical measurements for PBDB-T-SF point to an increase in order in the film morphology, which is in contrast to the reduction in order indicated by the absorption and out-of-plane GIXRD measurements. We believe this increase in order is in the in-plane arrangement of the PBDB-T-SF, indicating an increase in the order in the conjugated backbone or alkyl stacking direction with a decrease in order in the π-π stacking direction.

Increases in Young's modulus and hardness can be attributed to the formation of a denser and more crystalline structure in the films. This can be due to the fact that phase separation during the film formation can lead to an increase in intermolecular interactions between the polymer chains, resulting in the formation of more ordered crystalline domains. These domains can contribute to the mechanical stiffness and hardness of the film. However, it's important to note that the effect of toluene as a secondary solvent on the mechanical properties of conductive polymer films can be influenced by several factors, including the concentration of the solution, the rate of solvent evaporation, and the type of substrate used. Additionally, the use of other secondary solvents or poor solvents can lead to different morphologies and mechanical properties. Therefore, it's important to carefully consider the processing conditions and the desired properties when choosing secondary solvents for thin film fabrication. On comparing the results from the UV–visible absorption and GIXRD bulk/ensemble measurements to the AFM Young's Modulus results, it is apparent that a complex relationship exists that is polymer dependent (Table S2). In some cases, there is agreement between the techniques, as in the case of P3HT. However, for PBDB-T-SF, a reduction in π-π stacking is indicated by the absorption and GIXRD data, while the Young's Modulus in the AFM data exhibits a clear increase, suggesting increased order or crystallinity, possibly in the in-plane direction. Finally, for PCBTBT, while no changes were observed in UV–visible absorption and GIXRD data, nor in film roughness and feature size, the AFM Young's Modulus data showed clear changes in the nanomechanical properties of the film. This indicates that nanomechanical properties can change during processing without other detectable changes in the optical properties or chain order.

4. Conclusion

In this paper, we investigated how the nanomechanical properties of conjugated polymer thin films relate to their physical and optical properties for both pristine and solvent-treated thin films. The

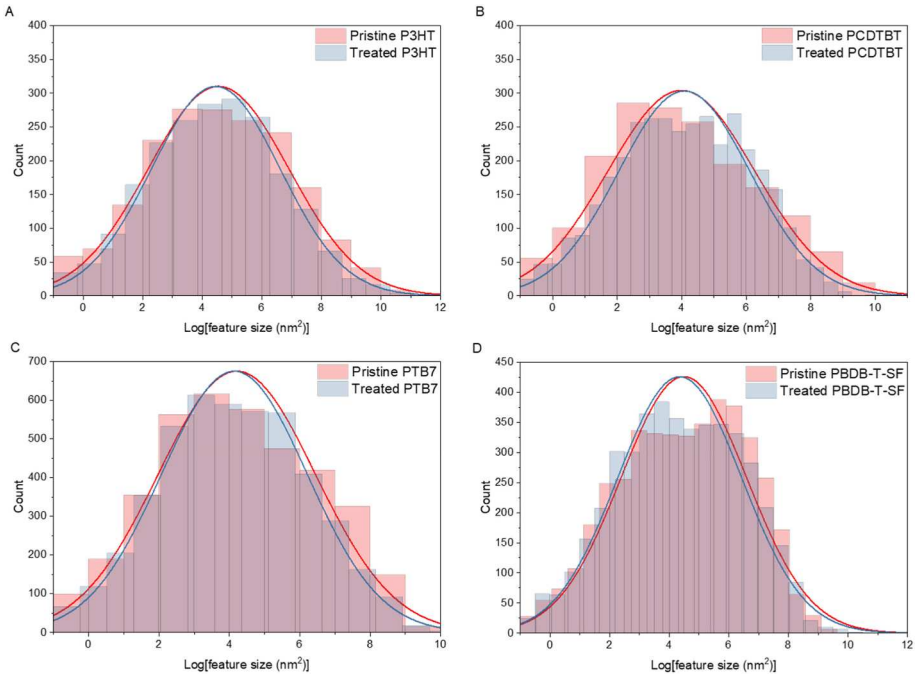

Fig. 9. Feature size analysis for pristine (red) and treated (blue) P3HT, PCDTBT, PTB7, and PBDB-T-SF films. Normal distributions fit to the log of the feature size. To account for differences in the number of values, bin sizes of each histogram were selected to directly compare the maximum of the distribution for each pristine and treated pair. (For interpretation of the references to color in this figure legend, the reader is referred to the Web version of this article.)

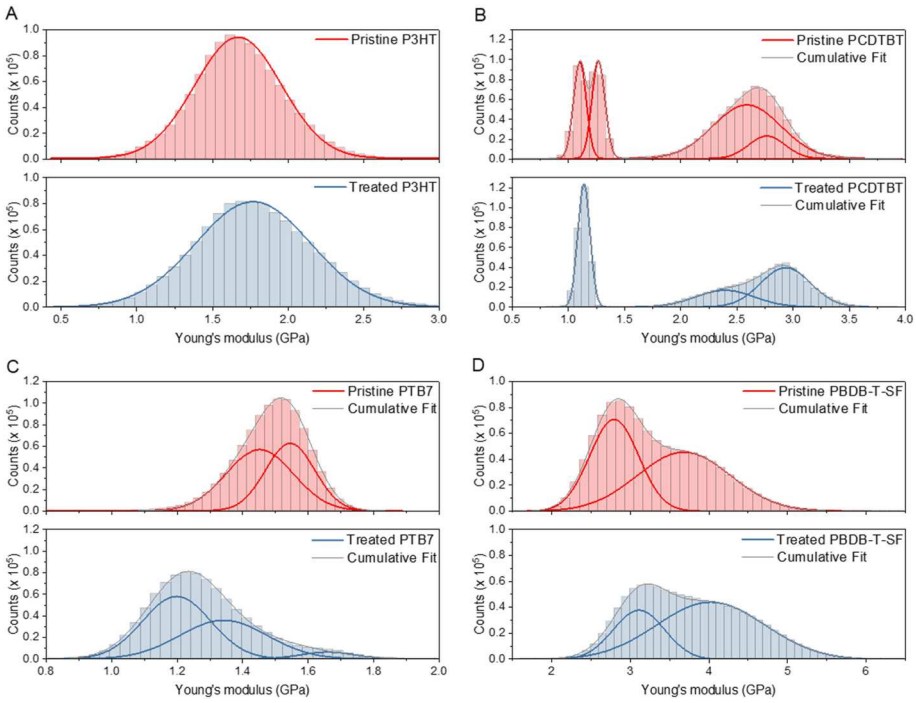

Fig. 10. Young's modulus analysis for pristine (red) and treated (blue) A) P3HT, B) PCDTBT, C) PTB7, and D) PBDB-T-SF films. To account for variations in the film and AFM measurements, a histogram was prepared of the calculated Young's modulus at each pixel of the images (256 × 256 pixels) for a minimum of 16 images in four different areas for each film. The histograms were fit with Gaussian peaks using the multiple peak fitting tool from OriginLab [116]. (For interpretation of the references to color in this figure legend, the reader is referred to the Web version of this article.)

application of a secondary solvent treatment during the spin coating process was shown to alter the properties of P3HT, PTB7, and PBDB-T-SF thin films, resulting in subtle changes in film quality and crystallinity. The effect on the most amorphous polymer, PCDTBT, was minimal based on bulk thin-film measurements (absorption and GIXRD); yet AFM nanomechanical measurements detected clear changes in Young's Modulus arising from the treatment. However, since the treated films of PCDTBT and PTB7 were less than half the thickness of the pristine films, toluene appeared to be a relatively good solvent for these polymers, resulting in film removal during spin coating and convoluting

characterization of film morphology due to potential substrate effects. For P3HT, subtle improvements in the crystallinity were detected due to the secondary solvent treatment, along with an improvement in the film quality (reduction in nanoscale roughness). Additionally, for P3HT, the data from AFM nanomechanical measurements agreed with changes in the absorption and GIXRD data caused by the secondary solvent treatment. In contrast, for PBDB-T-SF the AFM nanomechanical results indicated an increase in order in the conjugated backbone or alkyl chain direction along with an improvement in overall film quality, while bulk measurements indicated a reduction in order in the π-π stacking direction. Overall, these findings contribute to a better understanding of the impact of dynamic secondary solvent treatment on the nanomechanical properties of conjugated polymer thin films, and highlight the relevance of AFM-based nanomechanical characterization as an additional, complementary tool for characterizing order in conjugated polymer films.

CRediT authorship contribution statement

Krystal L. House: conceived the idea and co-wrote the manuscript, fabricated the samples, conducted the absorption spectroscopy, AFM measurements, and analyzed and interpreted the data. **Kent H. Christian:** assisted with the acquisition of the nanoindentation data and its interpretation. **Haydee Pacheco:** co-wrote the manuscript and assisted with data analysis and interpretation. **Richard A. Haber:** assisted with the acquisition of the nanoindentation data and its interpretation. **Deirdre M. O'Carroll:** conceived the idea and co-wrote the manuscript, supervised the work and assisted with data interpretation. Thomas J. Emge: acquired the GIXRD data and assisted with writing the GIXRD-related components of the paper.

Declaration of competing interest

The authors declare that they have no known competing financial interests or personal relationships that could have appeared to influence the work reported in this paper.

Data availability

Data will be made available on request.

Appendix A. Supplementary data

Supplementary data to this article can be found online at https://doi.org/10.1016/j.polymer.2023.126625.

References

[1] J.W. Jeong, G. Jo, S. Choi, Y.A. Kim, H. Yoon, S.-W. Ryu, J. Jung, M. Chang, Solvent additive-assisted anisotropic assembly and enhanced charge transport of π-conjugated polymer thin films, ACS Appl. Mater. Interfaces 10 (21) (2018) 18131–18140.

[2] P.J. Brown, D.S. Thomas, A. Köhler, J.S. Wilson, J.-S. Kim, C.M. Ramsdale, H. Sirringhaus, R.H. Friend, Effect of interchain interactions on the absorption and emission of poly(3-hexylthiophene), Phys. Rev. B 67 (6) (2003) 064203, https://doi.org/10.1103/PhysRevB.67.064203.

[3] R. Street, J. Northrup, A. Salleo, Transport in polycrystalline polymer thin-film transistors, Phys. Rev. B 71 (16) (2005) 165202.

[4] S. Goffri, C. Müller, N. Stingelin-Stutzmann, D.W. Breiby, C.P. Radano, J. W. Andreasen, R. Thompson, R.A. Janssen, M.M. Nielsen, P. Smith, Multicomponent semiconducting polymer systems with low crystallization-induced percolation threshold, Nat. Mater. 5 (12) (2006) 950–956.

[5] D. Venkateshvaran, M. Nikolka, A. Sadhanala, V. Lemaur, M. Zelazny, M. Kepa, M. Hurhangee, A.J. Kronemeijer, V. Pecunia, I. Nasrallah, Approaching disorder-free transport in high-mobility conjugated polymers, Nature 515 (7527) (2014) 384–388.

[6] V. Coropceanu, J. Cornil, D.A. da Silva Filho, Y. Olivier, R. Silbey, J.-L. Brédas, Charge transport in organic semiconductors, Chem. Rev. 107 (4) (2007) 926–952, https://doi.org/10.1021/cr050140x.

[7] R.A. Street, J.E. Northrup, A. Salleo, Transport in polycrystalline polymer thin-film transistors, Phys. Rev. B 71 (16) (2005) 165202, https://doi.org/10.1103/PhysRevB.71.165202.

[8] N. Vukmirović, L.-W. Wang, Charge carrier motion in disordered conjugated polymers: a multiscale Ab initio study, Nano Lett. 9 (12) (2009) 3996–4000, https://doi.org/10.1021/nl9021539.

[9] A. Salleo, Charge transport in polymeric transistors, Mater. Today 10 (3) (2007) 38–45, https://doi.org/10.1016/S1369-7021(07)70018-4.

[10] H. Sirringhaus, P.J. Brown, R.H. Friend, M.M. Nielsen, K. Bechgaard, B.M. W. Langeveld-Voss, A.J.H. Spiering, R.A.J. Janssen, E.W. Meijer, P. Herwig, et al., Two-dimensional charge transport in self-organized, high-mobility conjugated polymers, Nature 401 (6754) (1999) 685–688, https://doi.org/10.1038/44359.

[11] C.C. Mattheus, G.A. de Wijs, R.A. de Groot, T.T.M. Palstra, Modeling the polymorphism of pentacene, J. Am. Chem. Soc. 125 (20) (2003) 6323–6330, https://doi.org/10.1021/ja0211499.

[12] A.M. Hiszpanski, Y.-L. Loo, Directing the film structure of organic semiconductors via post-deposition processing for transistor and solar cell applications, Energy Environ. Sci. 7 (2) (2014) 592–608.

[13] H. Dong, W. Hu, Multilevel investigation of charge transport in conjugated polymers, Acc. Chem. Res. 49 (11) (2016) 2435–2443.

[14] Y. Diao, B.C. Tee, G. Giri, J. Xu, D.H. Kim, H.A. Becerril, R.M. Stoltenberg, T. H. Lee, G. Xue, S.C. Mannsfeld, Solution coating of large-area organic semiconductor thin films with aligned single-crystalline domains, Nat. Mater. 12 (7) (2013) 665–671.

[15] E. Mohammadi, C. Zhao, Y. Meng, G. Qu, F. Zhang, X. Zhao, J. Mei, J.-M. Zuo, D. Shukla, Y. Diao, Dynamic-template-directed multiscale assembly for large-area coating of highly-aligned conjugated polymer thin films, Nat. Commun. 8 (1) (2017) 1–11.

[16] S.G. Bucella, A. Luzio, E. Gann, L. Thomsen, C.R. McNeill, G. Pace, A. Perinot, Z. Chen, A. Facchetti, M. Caironi, Macroscopic and high-throughput printing of aligned nanostructured polymer semiconductors for MHz large-area electronics, Nat. Commun. 6 (1) (2015) 1–10.

[17] H.-R. Tseng, L. Ying, B.B. Hsu, L.A. Perez, C.J. Takacs, G.C. Bazan, A.J. Heeger, High mobility field effect transistors based on macroscopically oriented regioregular copolymers, Nano Lett. 12 (12) (2012) 6353–6357.

[18] F. Zhang, X. Dai, W. Zhu, H. Chung, Y. Diao, Large modulation of charge carrier mobility in doped nanoporous organic transistors, Adv. Mater. 29 (27) (2017) 1700411.

[19] S. Schott, E. Gann, L. Thomsen, S.H. Jung, J.K. Lee, C.R. McNeill, H. Sirringhaus, Charge-transport anisotropy in a uniaxially aligned diketopyrrolopyrrole-based copolymer, Adv. Mater. 27 (45) (2015) 7356–7364.

[20] G. Qu, X. Zhao, G.M. Newbloom, F. Zhang, E. Mohammadi, J.W. Strzalka, L. D. Pozzo, J. Mei, Y. Diao, Understanding interfacial alignment in solution coated conjugated polymer thin films, ACS Appl. Mater. Interfaces 9 (33) (2017) 27863–27874.

[21] G. Giri, E. Verploegen, S.C. Mannsfeld, S. Atahan-Evrenk, D.H. Kim, S.Y. Lee, H. A. Becerril, A. Aspuru-Guzik, M.F. Toney, Z. Bao, Tuning charge transport in solution-sheared organic semiconductors using lattice strain, Nature 480 (7378) (2011) 504–508.

[22] R. Noriega, J. Rivnay, K. Vandewal, F.P. Koch, N. Stingelin, P. Smith, M.F. Toney, A. Salleo, A general relationship between disorder, aggregation and charge transport in conjugated polymers, Nat. Mater. 12 (11) (2013) 1038–1044.

[23] Y. Diao, Y. Zhou, T. Kurosawa, L. Shaw, C. Wang, S. Park, Y. Guo, J.A. Reinspach, K. Gu, X. Gu, Flow-enhanced solution printing of all-polymer solar cells, Nat. Commun. 6 (1) (2015) 1–10.

[24] I. McCulloch, M. Heeney, C. Bailey, K. Genevicius, I. MacDonald, M. Shkunov, D. Sparrowe, S. Tierney, R. Wagner, W. Zhang, Liquid-crystalline semiconducting polymers with high charge-carrier mobility, Nat. Mater. 5 (4) (2006) 328–333.

[25] M. Halik, H. Klauk, U. Zschieschang, G. Schmid, C. Dehm, M. Schütz, S. Maisch, F. Effenberger, M. Brunnbauer, F. Stellacci, Low-voltage organic transistors with an amorphous molecular gate dielectric, Nature 431 (7011) (2004) 963–966, https://doi.org/10.1038/nature02987.

[26] A. Facchetti, M.-H. Yoon, T.J. Marks, Gate dielectrics for organic field-effect transistors: new opportunities for organic electronics, Adv. Mater. 17 (14) (2005) 1705–1725, https://doi.org/10.1002/adma.200500517.

[27] J.H. Cho, J. Lee, Y. Xia, B. Kim, Y. He, M.J. Renn, T.P. Lodge, C. Daniel Frisbie, Printable ion-gel gate dielectrics for low-voltage polymer thin-film transistors on plastic, Nat. Mater. 7 (11) (2008) 900–906, https://doi.org/10.1038/nmat2291.

[28] H. Sirringhaus, N. Tessler, R.H. Friend, Integrated, high-mobility polymer field-effect transistors driving polymer light-emitting diodes, Synth. Met. 102 (1) (1999) 857–860, https://doi.org/10.1016/S0379-6779(98)00365-8.

[29] L.-L. Chua, J. Zaumseil, J.-F. Chang, E.C.W. Ou, P.K.H. Ho, H. Sirringhaus, R. H. Friend, General observation of n-type field-effect behaviour in organic semiconductors, Nature 434 (7030) (2005) 194–199, https://doi.org/10.1038/nature03376.

[30] L. Bürgi, T. Richards, R. Friend, H. Sirringhaus, Close look at charge carrier injection in polymer field-effect transistors, J. Appl. Phys. 94 (9) (2003) 6129–6137.

[31] H.N. Tsao, K. Müllen, Improving polymer transistor performance via morphology control, Chem. Soc. Rev. 39 (7) (2010) 2372–2386, https://doi.org/10.1039/B918151M.

[32] O. Dolynchuk, P. Schmode, M. Fischer, M. Thelakkat, T. Thurn-Albrecht, Elucidating the effect of interfacial interactions on crystal orientations in thin films of polythiophenes, Macromolecules 54 (12) (2021) 5429–5439, https://doi.org/10.1021/acs.macromol.0c02510.

[33] E. Mohammadi, G. Qu, P. Kafle, S.-H. Jung, J.-K. Lee, Y. Diao, Design rules for dynamic-template-directed crystallization of conjugated polymers, Molecular Systems Design & Engineering 5 (1) (2020) 125–138, https://doi.org/10.1039/C9ME00042A.

[34] H.G. Kassa, J. Stuyver, A.-J. Bons, D.B. Haviland, P.-A. Thorén, R. Borgani, D. Forchheimer, P. Leclère, Nano-mechanical properties of interphases in dynamically vulcanized thermoplastic alloy, Polymer 135 (2018) 348–354.

[35] Z.-F. Yao, Z.-Y. Wang, H.-T. Wu, Y. Lu, Q.-Y. Li, L. Zou, J.-Y. Wang, J. Pei, Ordered solid-state microstructures of conjugated polymers arising from solution-state aggregation, Angew. Chem. Int. Ed. 59 (40) (2020) 17467–17471, https://doi.org/10.1002/anie.202007589, 2023/05/08.

[36] M. Gao, W. Wang, J. Hou, L. Ye, Control of aggregated structure of photovoltaic polymers for high-efficiency solar cells, Aggregate 2 (5) (2021) e46, https://doi.org/10.1002/agt2.46, 2023/05/08.

[37] H. Maddali, K.L. House, T.J. Emge, D.M. O'Carroll, Identification of the local electrical properties of crystalline and amorphous domains in electrochemically doped conjugated polymer thin films, RSC Adv. 10 (36) (2020) 21454–21463.

[38] J.Y. Na, M. Kim, Y.D. Park, Solution processing with a good solvent additive for highly reliable organic thin-film transistors, J. Phys. Chem. C 121 (25) (2017) 13930–13937.

[39] A.R. Aiyar, J.-I. Hong, J. Izumi, D. Choi, N. Kleinhenz, E. Reichmanis, Ultrasound-induced ordering in poly (3-hexylthiophene): role of molecular and process parameters on morphology and charge transport, ACS Appl. Mater. Interfaces 5 (7) (2013) 2368–2377.

[40] M. Chang, D. Choi, G. Wang, N. Kleinhenz, N. Persson, B. Park, E. Reichmanis, Photoinduced anisotropic assembly of conjugated polymers in insulating polymer blends, ACS Appl. Mater. Interfaces 7 (25) (2015) 14095–14103.

[41] J.S. Kim, J.H. Lee, J.H. Park, C. Shim, M. Sim, K. Cho, High-efficiency organic solar cells based on preformed poly (3-hexylthiophene) nanowires, Adv. Funct. Mater. 21 (3) (2011) 480–486.

[42] T.M. Clarke, A.M. Ballantyne, J. Nelson, D.D. Bradley, J.R. Durrant, Free energy control of charge photogeneration in polythiophene/fullerene solar cells: the influence of thermal annealing on P3HT/PCBM blends, Adv. Funct. Mater. 18 (24) (2008) 4029–4035.

[43] J.H. Park, J.S. Kim, J.H. Lee, W.H. Lee, K. Cho, Effect of annealing solvent solubility on the performance of poly (3-hexylthiophene)/methanofullerene solar cells, J. Phys. Chem. C 113 (40) (2009) 17579–17584.

[44] G. Jo, J. Jung, M. Chang, Controlled self-assembly of conjugated polymers via a solvent vapor pre-treatment for use in organic field-effect transistors, Polymers 11 (2) (2019) 332.

[45] N.-K. Kim, E.-S. Shin, Y.-Y. Noh, D.-Y. Kim, A selection rule of solvent for highly aligned diketopyrrolopyrrole-based conjugated polymer film for high performance organic field-effect transistors, Org. Electron. 55 (2018) 6–14, https://doi.org/10.1016/j.orgel.2018.01.006.

[46] J.W. Jeong, G. Jo, S. Choi, Y.A. Kim, H. Yoon, S.W. Ryu, J. Jung, M. Chang, Solvent additive-assisted anisotropic assembly and enhanced charge transport of π-conjugated polymer thin films, ACS Appl. Mater. Interfaces 10 (21) (2018) 18131–18140, https://doi.org/10.1021/acsami.8b03221. Article.

[47] M. Chang, D. Choi, B. Fu, E. Reichmanis, Solvent based hydrogen bonding: impact on poly (3-hexylthiophene) nanoscale morphology and charge transport characteristics, ACS Nano 7 (6) (2013) 5402–5413.

[48] Y.D. Park, H.S. Lee, Y.J. Choi, D. Kwak, J.H. Cho, S. Lee, K. Cho, Solubility-induced ordered polythiophene precursors for high-performance organic thin-film transistors, Adv. Funct. Mater. 19 (8) (2009) 1200–1206.

[49] Y. Xi, C.M. Wolf, L.D. Pozzo, Self-assembly of donor–acceptor conjugated polymers induced by miscible 'poor'solvents, Soft Matter 15 (8) (2019) 1799–1812.

[50] R. Traiphol, N. Charoenthai, T. Srikhirin, T. Kerdcharoen, T. Osotchan, T. Maturos, Chain organization and photophysics of conjugated polymer in poor solvents: aggregates, agglomerates and collapsed coils, Polymer 48 (3) (2007) 813–826.

[51] R. Traiphol, R. Potai, N. Charoenthai, T. Srikhirin, T. Kerdcharoen, T. Osotchan, Effects of chain conformation and chain length on degree of aggregation in assembled particles of conjugated polymer in solvents–nonsolvent: a spectroscopic study, J. Polym. Sci. B Polym. Phys. 48 (8) (2010) 894–904.

[52] H. Chang, P. Wang, H. Li, J. Zhang, D. Yan, Solvent vapor assisted spin-coating: a simple method to directly achieve high mobility from P3HT based thin film transistors, Synth. Met. 184 (2013) 1–4.

[53] G.L. Schulz, S. Ludwigs, Controlled crystallization of conjugated polymer films from solution and solvent vapor for polymer electronics, Adv. Funct. Mater. 27 (1) (2017) 1603083.

[54] T.K. An, I. Kang, H.j. Yun, H. Cha, J. Hwang, S. Park, J. Kim, Y.J. Kim, D.S. Chung, S.K. Kwon, Solvent additive to achieve highly ordered nanostructural semicrystalline DPP copolymers: toward a high charge carrier mobility, Adv. Mater. 25 (48) (2013) 7003–7009.

[55] J. Chang, P. Sonar, Z. Lin, C. Zhang, J. Zhang, Y. Hao, J. Wu, Controlling aggregation and crystallization of solution processed diketopyrrolopyrrole based polymer for high performance thin film transistors by pre-metered slot die coating process, Org. Electron. 36 (2016) 113–119.

[56] Y. Yao, J. Hou, Z. Xu, G. Li, Y. Yang, Effects of solvent mixtures on the nanoscale phase separation in polymer solar cells, Adv. Funct. Mater. 18 (12) (2008) 1783–1789.

[57] M. Xiao, F. Huang, W. Huang, Y. Dkhissi, Y. Zhu, J. Etheridge, A. Gray-Weale, U. Bach, Y.B. Cheng, L. Spiccia, A fast deposition-crystallization procedure for highly efficient lead iodide perovskite thin-film solar cells, Angew. Chem. Int. Ed. 53 (37) (2014) 9898–9903.

[58] N.J. Jeon, J.H. Noh, Y.C. Kim, W.S. Yang, S. Ryu, S.I. Seok, Solvent engineering for high-performance inorganic–organic hybrid perovskite solar cells, Nat. Mater. 13 (9) (2014) 897–903.

[59] D. Prochowicz, M.M. Tavakoli, A. Solanki, T.W. Goh, K. Pandey, T.C. Sum, M. Saliba, P. Yadav, Understanding the effect of chlorobenzene and isopropanol anti-solvent treatments on the recombination and interfacial charge accumulation in efficient planar perovskite solar cells, J. Mater. Chem. A 6 (29) (2018) 14307–14314.

[60] J. Liu, N. Li, J. Jia, J. Dong, Z. Qiu, S. Iqbal, B. Cao, Perovskite films grown with green mixed anti-solvent for highly efficient solar cells with enhanced stability, Sol. Energy 181 (2019) 285–292.

[61] F. Yang, M.A. Kamarudin, P. Zhang, G. Kapil, T. Ma, S. Hayase, Enhanced crystallization by methanol additive in antisolvent for achieving high-quality MAPbI3 perovskite films in humid atmosphere, ChemSusChem 11 (14) (2018) 2348–2357.

[62] F. Li, J. Yuan, X. Ling, Y. Zhang, Y. Yang, S.H. Cheung, C.H.Y. Ho, X. Gao, W. Ma, A universal strategy to utilize polymeric semiconductors for perovskite solar cells with enhanced efficiency and longevity, Adv. Funct. Mater. 28 (15) (2018) 1706377.

[63] G. Jo, S.H. Cho, H. Kim, H. Yoon, S. Han, M. Chang, Impacts of secondary solvents on morphology and charge transport of conjugated polymer thin films, Org. Electron. 81 (2020) 105688.

[64] Z.K. Nagy, M. Fujiwara, R.D. Braatz, Modelling and control of combined cooling and antisolvent crystallization processes, J. Process Control 18 (9) (2008) 856–864, https://doi.org/10.1016/j.jprocont.2008.06.002.

[65] H. Yin, J. Yan, J.K.W. Ho, D. Liu, P. Bi, C.H.Y. Ho, X. Hao, J. Hou, G. Li, S.K. So, Observing electron transport and percolation in selected bulk heterojunctions bearing fullerene derivatives, non-fullerene small molecules, and polymeric acceptors, Nano Energy 64 (2019) 103950, https://doi.org/10.1016/j.nanoen.2019.103950.

[66] H.K. Nguyen, M. Ito, K. Nakajima, Elastic and viscoelastic characterization of inhomogeneous polymers by bimodal atomic force microscopy, Jpn. J. Appl. Phys. 55 (8S1) (2016) 08NB06.

[67] M. Chyasnavichyus, S.L. Young, V.V. Tsukruk, Probing of polymer surfaces in the viscoelastic regime, Langmuir 30 (35) (2014) 10566–10582, https://doi.org/10.1021/la404925h.

[68] R. Proksch, M. Kocun, D. Hurley, M. Viani, A. Labuda, W. Meinhold, J. Bemis, Practical loss tangent imaging with amplitude-modulated atomic force microscopy, J. Appl. Phys. 119 (13) (2016) 134901, https://doi.org/10.1063/1.4944879.

[69] J.S.d. Sousa, J.A.C. Santos, E.B. Barros, L.M.R. Alencar, W.T. Cruz, M.V. Ramos, J. M. Filho, Analytical model of atomic-force-microscopy force curves in viscoelastic materials exhibiting power law relaxation, J. Appl. Phys. 121 (3) (2017) 034901, https://doi.org/10.1063/1.4974043.

[70] P.D. Garcia, R. Garcia, Determination of the elastic moduli of a single cell cultured on a rigid support by force microscopy, Biophys. J. 114 (12) (2018) 2923–2932, https://doi.org/10.1016/j.bpj.2018.05.012.

[71] B. Rajabifar, J.M. Jadhav, D. Kiracofe, G.F. Meyers, A. Raman, Dynamic AFM on viscoelastic polymer samples with surface forces, Macromolecules 51 (23) (2018) 9649–9661, https://doi.org/10.1021/acs.macromol.8b01485.

[72] F. Crippa, P.-A. Thorén, D. Forchheimer, R. Borgani, B. Rothen-Rutishauser, A. Petri-Fink, D.B. Haviland, Probing nano-scale viscoelastic response in air and in liquid with dynamic atomic force microscopy, Soft Matter 14 (19) (2018) 3998–4006, https://doi.org/10.1039/C8SM00149A.

[73] D. Wang, T.P. Russell, Advances in atomic force microscopy for probing polymer structure and properties, Macromolecules 51 (1) (2018) 3–24, https://doi.org/10.1021/acs.macromol.7b01459.

[74] J. Martín, M. Muñoz, M. Encinar, M. Calleja, M. Martín-González, Fabrication and mechanical characterization of semi-free-standing (conjugated) polymer thin films, Langmuir 30 (18) (2014) 5217–5223, https://doi.org/10.1021/la4032267.

[75] S. Benaglia, C.A. Amo, R. Garcia, Fast, quantitative and high resolution mapping of viscoelastic properties with bimodal AFM, Nanoscale 11 (32) (2019) 15289–15297, https://doi.org/10.1039/C9NR04396A.

[76] S. Logothetidis, S. Kassavetis, C. Charitidis, Y. Panayiotatos, A. Laskarakis, Nanoindentation studies of multilayer amorphous carbon films, Carbon 42 (5–6) (2004) 1133–1136.

[77] H. Huang, I. Dobryden, P.-A. Thorén, L. Ejenstam, J. Pan, M. Fielden, D. Haviland, P.M. Claesson, Local surface mechanical properties of PDMS-silica nanocomposite probed with Intermodulation AFM, Compos. Sci. Technol. 150 (2017) 111–119.

[78] D. Ebeling, B. Eslami, S.D.J. Solares, Visualizing the subsurface of soft matter: simultaneous topographical imaging, depth modulation, and compositional mapping with triple frequency atomic force microscopy, ACS Nano 7 (11) (2013) 10387–10396.

[79] J. George, L.B. Azad, A.M. Poulose, Y. An, A.K. Sarmah, Nano-mechanical behaviour of biochar-starch polymer composite: investigation through advanced dynamic atomic force microscopy, Compos. Appl. Sci. Manuf. 124 (2019) 105486.

[80] M. Kocun, A. Labuda, W. Meinhold, I. Revenko, R. Proksch, Fast, high resolution, and wide modulus range nanomechanical mapping with bimodal tapping mode, ACS Nano 11 (10) (2017) 10097–10105.

[81] R. Giridharagopal, L. Flagg, J. Harrison, M. Ziffer, J. Onorato, C. Luscombe, D. Ginger, Electrochemical strain microscopy probes morphology-induced variations in ion uptake and performance in organic electrochemical transistors, Nat. Mater. 16 (7) (2017) 737–742.

[82] M.E. McConney, S. Singamaneni, V.V. Tsukruk, Probing soft matter with the atomic force microscopies: imaging and force spectroscopy, Polym. Rev. 50 (3) (2010) 235–286, https://doi.org/10.1080/15583724.2010.493255.

[83] V. Panchal, I. Dobryden, U.D. Hangen, D. Simatos, L.J. Spalek, I.E. Jacobs, G. Schweicher, P.M. Claesson, D. Venkateshvaran, Mechanical properties of

organic electronic polymers on the nanoscale, Advanced Electronic Materials (2021) 2101019.
[84] C.M. Hansen, Hansen Solubility Parameters: a User's Handbook, CRC press, 2007.
[85] J.H. Hildebrand, R.L. Scott, Regular Solutions, Prentice-Hall, Inc., 1962.
[86] J.H. Hildebrand, R.L. Scott, The Solubility of Nonelectrolytes, Reinhold Publishing Corporation, 1950.
[87] F. Machui, S. Abbott, D. Waller, M. Koppe, C.J. Brabec, Determination of solubility parameters for organic semiconductor formulations, Macromol. Chem. Phys. 212 (19) (2011) 2159–2165, https://doi.org/10.1002/macp.201100284.
[88] F. Machui, S. Langner, X. Zhu, S. Abbott, C.J. Brabec, Determination of the P3HT: PCBM solubility parameters via a binary solvent gradient method: impact of solubility on the photovoltaic performance, Sol. Energy Mater. Sol. Cell. 100 (2012) 138–146.
[89] D.T. Duong, B. Walker, J. Lin, C. Kim, J. Love, B. Purushothaman, J.E. Anthony, T.Q. Nguyen, Molecular solubility and hansen solubility parameters for the analysis of phase separation in bulk heterojunctions, J. Polym. Sci. B Polym. Phys. 50 (20) (2012) 1405–1413.
[90] B. Walker, A. Tamayo, D.T. Duong, X.D. Dang, C. Kim, J. Granstrom, T. Q. Nguyen, A systematic approach to solvent selection based on cohesive energy densities in a molecular bulk heterojunction system, Adv. Energy Mater. 1 (2) (2011) 221–229.
[91] D.W. Van Krevelen, K. Te Nijenhuis, Properties of Polymers: Their Correlation with Chemical Structure; Their Numerical Estimation and Prediction from Additive Group Contributions, Elsevier, 2009.
[92] D. Leman, M.A. Kelly, S. Ness, S. Engmann, A. Herzing, C. Snyder, H.W. Ro, R. J. Kline, D.M. DeLongchamp, L.J. Richter, In situ characterization of polymer–fullerene bilayer stability, Macromolecules 48 (2) (2015) 383–392.
[93] A.F. Barton, CRC Handbook of Solubility Parameters and Other Cohesion Parameters, Routledge, 2017.
[94] G. Zhang, M. McBride, N. Persson, S. Lee, T.J. Dunn, M.F. Toney, Z. Yuan, Y.-H. Kwon, P.-H. Chu, B. Risteen, et al., Versatile interpenetrating polymer network approach to robust stretchable electronic devices, Chem. Mater. 29 (18) (2017) 7645–7652, https://doi.org/10.1021/acs.chemmater.7b03019.
[95] S. Strohm, F. Machui, S. Langner, P. Kubis, N. Gasparini, M. Salvador, I. McCulloch, H.J. Egelhaaf, C.J. Brabec, P3HT: non-fullerene acceptor based large area, semi-transparent PV modules with power conversion efficiencies of 5%, processed by industrially scalable methods, Energy Environ. Sci. 11 (8) (2018) 2225–2234, https://doi.org/10.1039/C8EE01150H.
[96] W.C. Oliver, G.M. Pharr, An improved technique for determining hardness and elastic modulus using load and displacement sensing indentation experiments, J. Mater. Res. 7 (6) (1992) 1564–1583.
[97] M. Krumova, A. Flores, F.B. Calleja, S. Fakirov, Elastic properties of oriented polymers, blends and reinforced composites using the microindentation technique, Colloid Polym. Sci. 280 (7) (2002) 591–598.
[98] L. Shen, L. Wang, T. Liu, C. He, Nanoindentation and morphological studies of epoxy nanocomposites, Macromol. Mater. Eng. 291 (11) (2006) 1358–1366.
[99] H.-C. Li, K.K. Rao, J.-Y. Jeng, Y.-J. Hsiao, T.-F. Guo, Y.-R. Jeng, T.-C. Wen, Nano-scale mechanical properties of polymer/fullerene bulk hetero-junction films and their influence on photovoltaic cells, Sol. Energy Mater. Sol. Cell. 95 (11) (2011) 2976–2980.
[100] J.L. Hutter, J. Bechhoefer, Calibration of atomic-force microscope tips, Rev. Sci. Instrum. 64 (7) (1993) 1868–1873.
[101] J.E. Sader, J.W. Chon, P. Mulvaney, Calibration of rectangular atomic force microscope cantilevers, Rev. Sci. Instrum. 70 (10) (1999) 3967–3969.
[102] A. Labuda, J. Cleveland, N.A. Geisse, M. Kocun, B. Ohler, R. Proksch, M.B. Viani, D. Walters, Photothermal excitation for improved cantilever drive performance in tapping mode atomic force microscopy, Microsc. Anal. (2014) 21–25.
[103] D. Hurley, M. Kocun, I. Revenko, B. Ohler, R. Proksch, Fast, quantitative AFM nanomechanical measurements using AM-FM Viscoelastic Mapping Mode, Microsc. Anal. (2015) 9–13.
[104] M. Böckmann, T. Schemme, D.H. de Jong, C. Denz, A. Heuer, N.L. Doltsinis, Structure of P3HT crystals, thin films, and solutions by UV/Vis spectral analysis, Phys. Chem. Chem. Phys. 17 (43) (2015) 28616–28625, https://doi.org/10.1039/C5CP03665H.
[105] L. Cartwright, H. Yi, A. Iraqi, Effect of fluorination pattern and extent on the properties of PCDTBT derivatives, New J. Chem. 40 (2) (2016) 1655–1662, https://doi.org/10.1039/C5NJ02394G.
[106] C. Duan, W. Cai, B.B.Y. Hsu, C. Zhong, K. Zhang, C. Liu, Z. Hu, F. Huang, G. C. Bazan, A.J. Heeger, et al., Toward green solvent processable photovoltaic materials for polymer solar cells: the role of highly polar pendant groups in charge carrier transport and photovoltaic behavior, Energy Environ. Sci. 6 (10) (2013) 3022–3034, https://doi.org/10.1039/C3EE41838C.
[107] P. Ehrenreich, S.T. Birkhold, E. Zimmermann, H. Hu, K.-D. Kim, J. Weickert, T. Pfadler, L. Schmidt-Mende, H-aggregate analysis of P3HT thin films-Capability and limitation of photoluminescence and UV/Vis spectroscopy, Sci. Rep. 6 (1) (2016) 32434, https://doi.org/10.1038/srep32434.
[108] N. Kiriy, E. Jähne, H.-J. Adler, M. Schneider, A. Kiriy, G. Gorodyska, S. Minko, D. Jehnichen, P. Simon, A.A. Fokin, et al., One-Dimensional aggregation of regioregular polyalkylthiophenes, Nano Lett. 3 (6) (2003) 707–712, https://doi.org/10.1021/nl0341032.
[109] T. Supasai, V. Amornkitbamrung, C. Thanachayanont, I.M. Tang, T. Sutthibutpong, N. Rujisamphan, Visualizing nanoscale phase morphology for understanding photovoltaic performance of PTB7: PC71BM solar cell, Appl. Surf. Sci. 422 (2017) 509–517, https://doi.org/10.1016/j.apsusc.2017.05.205.
[110] D.T. Duong, C. Wang, E. Antono, M.F. Toney, A. Salleo, The chemical and structural origin of efficient p-type doping in P3HT, Org. Electron. 14 (5) (2013) 1330–1336.
[111] Q. Zafar, K. Sulaiman, Utility of PCDTBT polymer for the superior sensing parameters of electrical response based relative humidity sensor, React. Funct. Polym. 105 (2016) 45–51, https://doi.org/10.1016/j.reactfunctpolym.2016.05.014.
[112] N. Blouin, A. Michaud, D. Gendron, S. Wakim, E. Blair, R. Neagu-Plesu, M. Belletete, G. Durocher, Y. Tao, M. Leclerc, Toward a rational design of poly (2, 7-carbazole) derivatives for solar cells, J. Am. Chem. Soc. 130 (2) (2008) 732–742.
[113] S. Chae, K.H. Cho, S. Won, A. Yi, J. Choi, H.H. Lee, J.-H. Kim, H.J. Kim, Favorable face-on orientation of a conjugated polymer on roll-to-roll-transferred graphene interface, Adv. Mater. Interfac. 4 (23) (2017) 1701099, https://doi.org/10.1002/admi.201701099.
[114] M.R. Hammond, R.J. Kline, A.A. Herzing, L.J. Richter, D.S. Germack, H.-W. Ro, C. L. Soles, D.A. Fischer, T. Xu, L. Yu, et al., Molecular order in high-efficiency polymer/fullerene bulk heterojunction solar cells, ACS Nano 5 (10) (2011) 8248–8257, https://doi.org/10.1021/nn202951e.
[115] B. Kan, H. Feng, H. Yao, M. Chang, X. Wan, C. Li, J. Hou, Y. Chen, A chlorinated low-bandgap small-molecule acceptor for organic solar cells with 14.1% efficiency and low energy loss, Sci. China Chem. 61 (10) (2018) 1307–1313, https://doi.org/10.1007/s11426-018-9334-9.
[116] OriginLab Corporation: Northampton, MA, USA, 2021.
[117] B. O'Connor, E.P. Chan, C. Chan, B.R. Conrad, L.J. Richter, R.J. Kline, M. Heeney, I. McCulloch, C.L. Soles, D.M. DeLongchamp, Correlations between mechanical and electrical properties of polythiophenes, ACS Nano 4 (12) (2010) 7538–7544.
[118] P. Karagiannidis, S. Kassavetis, C. Pitsalidis, S. Logothetidis, Thermal annealing effect on the nanomechanical properties and structure of P3HT: PCBM thin films, Thin Solid Films 519 (12) (2011) 4105–4109.
[119] ImageJ, National Institutes of Health: Bethesda, Maryland, USA, 1997-2008. https://imagej.nih.gov/ij/.
[120] I. Dobryden, V.V. Korolkov, V. Lemaur, M. Waldrip, H.-I. Un, D. Simatos, L. J. Spalek, O.D. Jurchescu, Y. Olivier, P.M. Claesson, et al., Dynamic self-stabilization in the electronic and nanomechanical properties of an organic polymer semiconductor, Nat. Commun. 13 (1) (2022) 3076, https://doi.org/10.1038/s41467-022-30801-x.
[121] B. Rajabifar, A. Bajaj, R. Reifenberger, R. Proksch, A. Raman, Discrimination of adhesion and viscoelasticity from nanoscale maps of polymer surfaces using bimodal atomic force microscopy, Nanoscale 13 (41) (2021) 17428–17441, https://doi.org/10.1039/D1NR03437E.
[122] C.A. Amo, A.P. Perrino, A.F. Payam, R. Garcia, Mapping elastic properties of heterogeneous materials in liquid with angstrom-scale resolution, ACS Nano 11 (9) (2017) 8650–8659, https://doi.org/10.1021/acsnano.7b04381.
[123] D.C. Hurley, S.E. Campbell, J.P. Killgore, L.M. Cox, Y. Ding, Measurement of viscoelastic loss tangent with contact resonance modes of atomic force microscopy, Macromolecules 46 (23) (2013) 9396–9402, https://doi.org/10.1021/ma401988h.
[124] D.G. Yablon, A. Gannepalli, R. Proksch, J. Killgore, D.C. Hurley, J. Grabowski, A. H. Tsou, Quantitative viscoelastic mapping of polyolefin blends with contact resonance atomic force microscopy, Macromolecules 45 (10) (2012) 4363–4370, https://doi.org/10.1021/ma2028038.
[125] H.K. Nguyen, M. Aoki, X. Liang, S. Yamamoto, K. Tanaka, K. Nakajima, Local mechanical properties of heterogeneous nanostructures developed in a cured epoxy network: implications for innovative adhesion technology, ACS Appl. Nano Mater. 4 (11) (2021) 12188–12196, https://doi.org/10.1021/acsanm.1c02692.